A series of lanthanide(III) metal-organic frameworks derived from pyridyl-dicarboxylate ligand: single-molecule magnet behaviour and luminescent properties

Received 00th January 20xx,
Accepted 00th January 20xx

DOI: 10.1039/x0xx00000x

www.rsc.org/

Chengcheng Zhang,[a‡] Xiufang Ma,[a‡] Peipei Cen,[c] Xiaoyong Jin,[a] Jinhui Yang,[a] Yi-Quan Zhang,[d*] Jesús Ferrando-Soria,[b] Emilio Pardo[b] and Xiangyu Liu[ae*]

The reactions of Ln^{III} ions with a versatile pyridyl-decorated dicarboxylic acid ligand lead to a series of novel three-dimensional (3D) Ln-MOFs, $[Ln_3(pta)_4(Hpta)(H_2O)]\cdot xH_2O$ (Ln = Dy (**1**), Eu (**2**), Gd (**3**), Tb (**4**), H_2pta = 2-(4-pyridyl)-terephthalic acid, x = 6 for **1**, 2.5 for **2**, 1.5 for **3** and 2 for **4**). The Ln^{3+} ions act as the nine-coordinated Muffin spheres, linking to each other to generate trinuclear $\{Ln_3(OOC)_6N_2\}$ SBUs, which are further extended to be interesting 3D topology architectures. To the best of our knowledge, the Dy-MOF exhibits a zero-field single-molecule magnet (SMM) behaviour with the largest effective energy barrier among the previously reported 3D MOF-based Dy-SMMs. The combined analyses of a dilution sample (**1@Y**) and *ab initio* calculation demonstrate that the thermally assisted slow relaxation is mainly attributed to the single-ion magnetism. Furthermore, fluorescence measurements reveal that H_2pta can sensitize Eu^{III} and Tb^{III} characteristic luminescence.

Introduction

Single-molecule magnets (SMMs) have attracted considerable attention in recent years across many fields, including chemistry, physics, and materials science.[1] Among the SMM family, lanthanide ions are widely used as excellent magnetic building blocks owing to their intrinsic large spin state and large magnetic anisotropy derived from spin-orbit coupling and the crystal field effect, which are not easily satisfied in transition-metal compounds.[2] In this regard, large magnetic moments and remarkable magnetic anisotropy of lanthanide ions, particularly the Dy^{3+} ion, have rendered them very useful for applications in the single-molecule magnet (SMM) field,[3] as both a large magnetic moment and an obvious magnetic anisotropy are necessary for a SMM, which may show magnetic bistability and quantum-tunnelling effects, and find applications in areas ranging from high-density information storage to quantum computer and spintronics.[4] Especially, a breakthrough has been made by Layfield and co-workers in Dy-SIMs, exhibiting magnetic hysteresis at temperatures up to 80 K and a high effective energy barrier of 1541 cm^{-1}.[5] However, most lanthanide-based SMMs are isolated polynuclear or mononuclear complexes, and most cases could be sensitive to air (moisture and oxygen) and highly unstable, hence very hard to handle in real applications.[6] From the viewpoint of this sign, the high dimensional lanthanide molecular system, namely, lanthanide metal-organic frameworks (Ln-MOFs), behaving as synchronously intriguing topology and SMMs behaviour have been underexplored.[7]

A limited number of researches stated and emphasized that Dy-based frameworks exhibit magnetization relaxation that is probably from the symmetry-related single-ion behaviour or magnetic interaction between metal ions.[7,8] To better understand the related mechanism causing slow magnetic relaxation, new magnetic Ln-MOF systems merit further exploration. According to hard-soft acid-base (HSAB) principle, lanthanide ion has a high affinity for oxygen atom, and carboxylate can generally cater for the oxophilic nature of lanthanide ions.[9] Additionally, the ability of carboxylate to take different binding modes fits well with the flexible coordination geometries of lanthanide ions, which is proven to be another advantage to build lanthanide-organic frameworks (LnOFs).[10] However, carboxylate-based LnMOFs with interesting magnetic behaviours are relatively rare, that is, few of them show clear thermal relaxation processes, which is probably due to the strong quantum tunneling magnetization.[11] Up until now, the energy barrier of documented carboxylate-based molecular nanomagnets has remained low, which is mainly attributed to the weak coordination field of carboxylate-based ligands.[8a,12] Although the construction of carboxylate-based lanthanide molecular nanomagnets with a high energy barrier remains a challenging task, continuous study based on the "framework" approach toward high-performant MOF-based magnetic materials would be a wise strategy.

Furthermore, because 4f transitions of lanthanide ions belong to inner-shell transitions and the emission spectra display narrow bandwidth ($\Delta\lambda$ < 10 nm), they have been extensively explored for applications in lighting, display, sensing, and optical devices.[13] It is well-known that Eu(III) and Tb(III) ions emit dominant red and green luminescence, respectively. These intrinsic luminescent features of lanthanides together with the unique advantages of MOFs offer hopeful prospects for designing novel luminescent materials with enhanced desired functionalities and high added values for specific applications. However, the f-f transitions of lanthanide ions are

[a.] *State Key Laboratory of High-efficiency Utilization of Coal and Green Chemical Engineering, National Demonstration Centre for Experimental Chemistry Education, College of Chemistry and Chemical Engineering, Ningxia University, Yinchuan 750021, China. Email: xiangyuliu432@126.com*
[b.] *Departamento de Química Inorgánica, Instituto de Ciencia Molecular (ICMOL), Universidad de Valencia, Paterna 46980, Valencia, Spain*
[c.] *College of Public Health and Management, Ningxia Medical University, Yinchuan 750021, China*
[d.] *Jiangsu Key Laboratory for NSLSCS, School of Physical Science and Technology, Nanjing Normal University, Nanjing 210023, China. E-mail: zhangyiquan@njnu.edu.cn*
[e.] *State Key Laboratory of Coordination Chemistry, Nanjing University, Nanjing, 210023, China*

Electronic Supplementary Information (ESI) available: CCDC 1961611 (**1**), 2019858 (**2**), 2019861 (**3**) and 2019863 (**4**). For ESI and crystallographic data in CIF or other electronic format see DOI: 10.1039/x0xx00000x

‡ These authors contributed equally to this work.

forbidden, and thus their direct excitation is unfavored.[13a] Existing studies demonstrate that the most common strategy to trigger lanthanide(III) luminescence is through excitation of a ligand chromophore that behaves as an antenna.[14]

Owing to rich coordination modes and oxygen atoms' high affinity to the Ln(III) ions, a novel asymmetric pyridyl-carboxylate organic spacer, 2-(4-pyridyl)-terephthalic acid (H_2pta), could be included in our perspective. As a result, four 3D Ln-MOFs have been successfully isolated, namely, $[Dy_3(pta)_4(Hpta)(H_2O)]\cdot 6H_2O$ (**1**), $[Eu_3(pta)_4(Hpta)(H_2O)]\cdot 2.5H_2O$ (**2**), $[Gd_3(pta)_4(Hpta)(H_2O)]\cdot 1.5H_2O$ (**3**) and $[Tb_3(pta)_4(Hpta)(H_2O)]\cdot 2H_2O$ (**4**), which possess rigid 3D skeletons consisting of trinuclear Ln(III) units. Remarkably, magnetic analysis reveals that as-prepared Dy-MOF presents slow magnetic relaxation of the SMM behaviour under zero dc field. Moreover, theoretical calculations and the magnetically diluted sample Dy/Y (**1@Y**) are crucial to elucidate the dynamic magnetic properties of **1**. Furthermore, the luminescent properties of **2** and **4** are investigated, showing characteristic emissions for Eu(III) and Tb(III) at room temperature, respectively.

Experimental

Materials and Physical Measurements

All reagents used for the synthesis were purchased from commercial sources and used without further purification. Elemental analyses of C, H and N were performed on a Vario EL III analyzer. Infrared (IR) spectra were recorded on a Bruker FTTR instrument with KBr pellets (4000-400cm^{-1}). Thermogravimetric analysis (TGA) was performed on a CDR-4P thermal analyzer of Shanghai Balance Instrument factory using dry oxygen-free nitrogen as the atmosphere with a flowing rate of 10 mL·min^{-1}. Powder X-ray diffraction (PXRD) experiments were recorded with a Rigaku RU200 diffractometer at 60 kV, 300 mA, and Cu Kα radiation (λ = 1.5406 Å), with a scan speed of 5° min^{-1} and a step size of 0.02° in 2ϑ. An accurate yttrium/dysprosium ratio was measured using the inductively coupled plasma (ICP) atomic emission spectra analyzed by a TJA IRIS(HR) spectrometry. All magnetization data were recorded with a Quantum Design SQUID magnetometer. The magnetic susceptibility data were corrected for the diamagnetic susceptibility by means of Pascal's constants and sample-holder calibration. The fluorescence spectra were obtained using a Hitachi F-7000 fluorescence spectrophotometer at room temperature. The fluorescence lifetime and the quantum yield were measured on a Bruker a300 Spectrofluorometer under excitation at 320 nm and 290nm.

Preparation of 1-4

Synthesis of $[Dy_3(pta)_4(Hpta)(H_2O)]\cdot 6H_2O$ (1) $DyCl_3\cdot 6H_2O$ (0.0094 g, 0.025 mmol), H_2pta (0.006 g, 0.025 mmol) were sequentially added into the mixture of H_2O (8 mL) and transferred to 25 mL Teflon-lined stainless steel autoclave. After being stirred in air for 30 min, the mixture was sealed 160 °C for 2 days, and then cooled to room temperature at a rate of 5 °C·h^{-1}. Colorless block crystals of **1** was collected by filtration. (yield: 0.059 g, 45%, based on Dy^{3+}). Anal. calcd for $C_{65}H_{50}Dy_3N_5O_{27}$ (1820.63): C, 42.88; H, 2.77; N, 3.85%. Found: C, 43.51; H, 2.98; N, 3.52%. Main IR features (KBr pellet, cm^{-1}): 3434 (w), 3028 (w), 2851 (w), 2498 (w), 1603 (s), 1594 (s), 1459 (w), 1441 (w), 1379 (m),1368 (m), 1352 (m), 1323 (m), 1025 (w), 893 (w), 794 (m), 619 (w), 537 (w).

Complexes **2**-**4** were prepared by means of the same methods that used for **1**, except $DyCl_3\cdot 6H_2O$ was replaced by $EuCl_3\cdot 6H_2O$, $GdCl_3\cdot 6H_2O$ and $TbCl_3\cdot 6H_2O$, respectively.

Synthesis of $[Eu_3(pta)_4(Hpta)(H_2O)]\cdot 2.5H_2O$ (2) Yield: 60%. Anal. calcd for $C_{65}H_{41}Eu_3N_5O_{23.5}$ (M = 1736.93). **2**: C 45.29, H 2.40, N 4.02%. Found: C 45.82, H 2.93, N 3.79%. IR data (KBr, cm^{-1}): 3413 (m), 2920 (w), 2850 (w), 2360 (w), 1639 (s), 1559 (s), 1522 (m), 1473 (m), 1371 (m), 1004 (w), 848 (m), 785 (m), 627 (w), 564 (w).

Synthesis of $[Gd_3(pta)_4(Hpta)(H_2O)]\cdot 1.5H_2O$ (3) Yield: 58%. Anal. calcd for $C_{65}H_{39}Gd_3N_5O_{22.5}$ (M = 1723.63). **3**: C 45.34, H 2.28, N 4.07%. Found: C 45.76, H 2.63, N 3.71%. IR data (KBr, cm^{-1}): 3414 (m), 3076 (w), 2852 (w), 2398 (w), 1636 (s), 1559 (s), 1457 (m), 1420 (w), 1384 (m),1317 (m), 1270 (m), 1072 (m), 1024 (w), 851 (w), 786 (m), 627 (w), 519 (w).

Synthesis of $[Tb_3(pta)_4(Hpta)(H_2O)]\cdot 2H_2O$ (4) Yield: 55%. Anal. calcd for $C_{65}H_{40}Tb_3N_5O_{23}$ (M = 1738.80). **4**: C 44.98, H 2.32, N 4.04%. Found: C 44.40, H 2.61, N 3.64%. IR data (KBr, cm^{-1}): 3447 (m), 3073 (w), 2920 (w), 2651 (w), 1653 (s), 1558 (s), 1428 (s), 1388 (s), 1316 (m),1078 (w), 851 (m), 787 (m), 668 (w), 491 (w).

Synthesis of dysprosium-doped yttrium samples 1@Y. The magnetically dilute sample **1@Y** was obtained by combining accurately measured amounts of $DyCl_3\cdot 6H_2O$ and $YCl_3\cdot 6H_2O$ in a 1:10 molar ratio, following the procedure described for complex **1**. The final ratios of Dy/Y in diluted samples were analyzed by ICP to be 1:10.91 for **1**. Elem anal. calcd for $C_{65}H_{50}Dy_{0.24}Y_{2.76}N_5O_{27}$ (1617.51): C, 48.27; H, 3.12; N, 4.33%. Found: C, 48.69; H, 3.43; N, 4.65%.

X-ray crystallography

Crystallographic data were collected with a Bruker SMART APEX-CCD-based diffractometer using graphite monochromated Mo-Kα radiation (λ = 0.71073 Å) at 296(2) K. Data processing and absorption corrections were accomplished using SAINT and SADABS[15]. The structures were determined by direct methods and refined against F^2 by full-matrix least-squares with SHELXTL-2018[16]. All nonhydrogen atoms were refined with anisotropic thermal parameters. The hydrogen atoms were set in calculated positions and refined with isotropic temperature factors. The diffraction contribution of

Table 1. Selected crystallographic data and structure refinement for **1**-**4**.

	1	**2**	**3**	**4**
Empirical formula	$C_{65}H_{36}Dy_3N_5O_{21}$	$C_{65}H_{36}Eu_3N_5O_{21}$	$C_{65}H_{36}Gd_3N_5O_{21}$	$C_{65}H_{36}Tb_3N_5O_{21}$
Formula weight	1710.60	1736.93	1723.63	1738.80
Temperature	100.01K	298K	298.0K	296K
Space group	*P*21/m	*P*21/m	*P*21/m	*P*21/m

a (Å)	11.4564(8)	11.520(2)	11.513(3)	11.477(5)
b (Å)	27.544(2)	27.700(5)	27.717(6)	27.659(13)
c (Å)	11.5369(7)	11.600(2)	11.592(3)	11.556(5)
α (°)	90	90	90	90
β (°)	101.261(6)	102.121(6)	102.164(7)	101.930(1)
γ (°)	90	90	90	90
V (Å^3)	3570.4(4)	3619.2(12)	3616.0(14)	3589.3(3)
Z	2	2	2	2
D (g/cm^3)	1.591	1.585	1.583	1.609
Mu (mm^{-1})	3.179	2.643	2.793	2.999
F(0 0 0)	1654.2	1692.0	1676.0	1694.0
Unique reflections	6688	8452	8437	8383
Observed reflections	5630	7966	7061	7564
R_{int}	0.0713	0.0386	0.0645	0.0464
Final *R* indices	R_1 =0.1091	R_1 =0.0292	R_1 =0.0429	R_1 =0.0266
[$I > 2\sigma(I)$]	wR_2 =0.2514	wR_2 =0.0757	wR_2 =0.1031	wR_2 =0.0667
R indices (all data)	R_1 =0.1244 wR_2 =0.2596	R_1 =0.0316 wR_2 =0.0769	R_1 =0.0532 wR_2 =0.1086	R_1 =0.0266 wR_2 =0.0692
Goodness-of-fit on F^2	1.208	1.137	1.050	1.079

the highly disordered solvent molecules located in the structure was eliminated by applying the program SQUEEZE implemented in PLATON. The final formula of **1**-**4** were ascertained by combining the crystallographic data, elemental microanalyses, and TGA data. The selected structural refinement results for complexes **1**-**4** were summarized in Table 1. Selected bond lengths and angles are listed in Tables S2-S8, respectively.

Computational details

For the three-dimensional structure of **1**, we extracted a three-core unit including three types of individual Dy^{III} fragments indicated as Dy1, Dy2 and Dy2A. Complete-active-space self-consistent field (CASSCF) calculations on individual Dy^{III} fragments for **1** on the basis of single-crystal X-ray determined geometry have been carried out with MOLCAS 8.4[17] program package. Each individual Dy^{III} fragment in **1** was calculated keeping the experimentally determined structure of the corresponding compound while replacing the neighboring Dy^{III} ions by diamagnetic Lu^{III}.

The basis sets for all atoms are atomic natural orbitals from the MOLCAS ANO-RCC library: ANO-RCC-VTZP for Dy^{III}; VTZ for close N and O; VDZ for distant atoms. The calculations employed the second order Douglas-Kroll-Hess Hamiltonian, where scalar relativistic contractions were taken into account in the basis set and the spin-orbit couplings were handled separately in the restricted active space state interaction (RASSI-SO) procedure. Active electrons in 7 active spaces include all *f* electrons (CAS (9 in 7 for Dy^{III})) in the CASSCF calculation. To exclude all the doubts, we calculated all the roots in the active space. We have mixed the maximum number of spin-free state which was possible with our hardware (all from 21 sextets, 128 from 224 quadruplets, 130 from 490 doublets). SINGLE_ANISO[18] program was used to obtain energy levels, *g* tensors, magnetic axes, *et al.,* based on the above CASSCF/RASSI-SO calculations.

Results and discussion

Structure description

Single-crystal X-ray crystallography studies reveal that complexes **1**-**4** are isostructural trinuclear structures that crystallize in the monoclinic space group $P2_1/m$ (Table 1). In order to show their structure in detail, complex **1** is described as an example. The asymmetric unit of **1** bears two Dy^{III} atoms (Dy1 with a half and Dy2 with a complete occupancy), two pta^{2-} ligands, a half of $Hpta^-$ ligand, a half of coordinated H_2O molecule and three free H_2O molecules. The Dy1/Dy2 atoms are nine-coordinate in the $\{DyO_9\}$ and $\{DyO_8N\}$ environments, correspondingly (Figure 1a). The Dy1 ion is bounded by two oxygen atoms (O1 and O1A) donors coming from two μ_4-pta^{2-} ligands, four carboxylate oxygen atoms (O5, O5A, O6 and O7) from two μ_4-$Hpta^-$ ligands, two carboxylate oxygen atoms (O11 and O11A) from two μ_3-pta^{2-} ligands and one water molecule (O12W). The Dy2 centre is surrounded by three carboxylate oxygen atoms (O2, O3 and O4) from two μ_4-pta^{2-} ligands, one oxygen atom (O5) from another μ_4-$Hpta^-$ ligand, four carboxylate oxygen atoms (O8, O9, O10 and O11) from two μ_3-pta^{2-} ligands and one nitrogen (N1) donor from one μ_4-pta^{2-} ligand. All the Dy-O and Dy-N bond lengths fall within the range for other dodecahedra complexes of Dy^{III} (Tables S1 and S2).[7a-7c] The calculation of the distorted degree of the $\{DyO_9\}$ and $\{DyO_8N\}$ polyhedrons for Dy1/Dy2, with respect to the ideal nine-vertex sphere, by using SHAPE program,[19] reveals that the DyO_9/DyO_8N combinations in **1** are intermediate between diverse coordination geometries (Table S9). The nine-coordinated Dy1 and Dy2 ions in **1** represent the uniform Muffin architecture with the same C_s symmetry, and the continuous shape measures (CShMs) values are determined to be 1.380 and 1.798, respectively (Figure 1b). In contrast, the relatively small CShM for the Dy1 ion corresponds to more ideal geometry. The ligand in the MOF performs three coordination modes, in which the carboxyl groups of H_2pta spacers adopts η^1:η^1-μ_1, η^1:η^2-μ_2, η^1:η^1-μ_2 and η^2:η^2-μ_3 modes to link with metal centers, respectively (Figure 2).

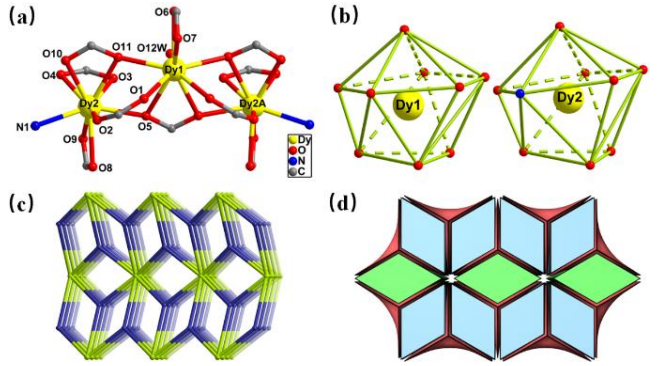

Figure 1. (a) Structure of secondary building unit in $[Dy_3(pta)_4(Hpta)(H_2O)]\cdot 6H_2O$. (b) Coordination polyhedral around Dy^{3+}. (c) Topological graph of **1**. (d) 3D tiling featured net of **1**. (Hydrogen atoms are omitted for clarity).

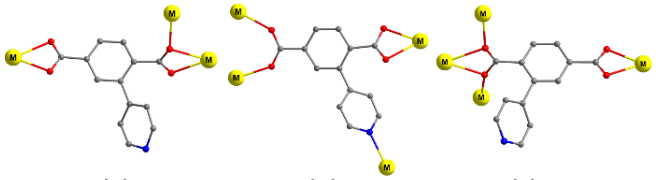

Figure 2. (a)-(c) are the coordination modes of the H_2pta ligands in **1**.

Each Dy(1) centre connects to two Dy(2) atoms via μ-carboxylate groups to form a trinuclear $\{Dy_3(OOC)_6N_2\}$ unit with Dy1···Dy2 distance of 4.070 Å, and the carboxylate groups of pta^{2-} ligands in the *syn-syn* bridging mode connect adjacent trinuclear Dy^{III} units to produce a one dimensional double-chain pattern along the *c* direction with a nearest intrachain Dy···Dy distance of 4.069 Å (Figure S2a). The adjacent 1D chains are combined by the pyridyl groups of μ_4-pta^{2-} ligands, resulting in a 2D layer parallel to the *bc* plane with the shortest interchain Dy···Dy distance of 8.012 Å. The adjacent layers are further linked by carboxylate oxygen atoms of $Hpta^-$ ligands, producing an interesting 3D framework (Figure S2b). Notably, TGA data shows that its main framework could remain unchanged until 450 °C (Figure 2b), indicating the outstanding thermostability of **1**. After simplified by using the software of TOPOS, **1** can be donated to be an unprecedented (3,8)-connected tfz-d topology with a point Schläfli symbol of {4^3}2{4^6.6^18.8^4}, where the pta^{2-} ligands are regarded as 3-connected nodes, the $Hpta^-$ ligands as linkers, and the trinuclear $\{Dy_3(OOC)_6N_2\}$ SBUs are considered as 8-connected nodes, respectively (Figure 1c). Further analysis of the tiling was also deal with the 3dt software to reflect the module building blocks, with the given tiling of 4[4.6^2]+2[6^3]+[4^2.6^2] = 2[4b.6d.6e]+2[4c.6g.6h]+2[6c.6e.6h]+[4a^2.6c^2] (transitivity: 2484) (Figure 1d).

PXRD and thermal gravimetric analysis (TGA)

The peak positions of the experimental PXRD patterns for **1**-**4** remain identical with their corresponding simulations based on single-crystal diffraction data at room temperature, indicating the good phase purity of the as-synthesized products (Figure 3a and S1). As can be seen in Figure 3a, pure crystalline phase of dilution sample (**1@Y**) was confirmed by Powder X-Ray diffraction. Also, the PXRD data of the activated samples at 200 °C are consistent with that of as-synthesized samples, indicating that the crystallinity of **1** is maintained after a loss of water molecules. Thermal analyses of Ln-MOFs **1**-**4** have been carried out in the temperature range of 25-700 °C under an inert atmosphere (maintained by a N_2 gas flow) at a heating rate of 10 °C min^{-1}, as shown in Figure 3b. The Ln-MOFs **1**-**4** being isostructural follow similar thermal decomposition patterns except for differences in the dehydration and decomposition temperatures. We have chosen **1** as a representative example for explaining the thermal stability and decomposition behaviour of assembled MOFs. The TGA curve of **1** suggests a typical two-step thermal decomposition pattern. For complex **1**, a total weight loss of 6.38% at 25−208 °C corresponds to the loss of $6H_2O$ guest molecules per formula unit (calc. 5.94%) and the further releases of coordinated H_2O molecules. Above 450 °C, the framework begins to collapse with the loss of other organic molecules.

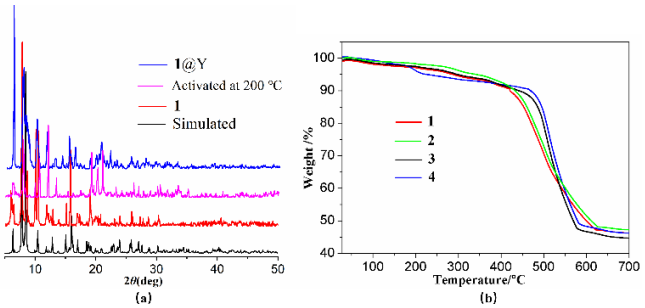

Figure 3. (a) Powder XRD pattern of **1**, **1@Y** and activated sample; (b) TGA plots of **1-4** under N_2 environment.

Magnetic studies

Direct current (dc) magnetic susceptibilities of **1**-**4** are measured in a 1000 Oe field in the range of 1.8-300 K (Figure 4 and S3). The room-temperature $\chi_M T$ products of 40.75 cm^3 K mol^{-1} for **1** and 35.31 cm^3 K mol^{-1} **4** are slightly lower than those for three isolated Ln^{III} ions, 42.51 cm^3 K mol^{-1} (Dy^{III}, $^6H_{15/2}$, g = 4/3) and 35.43 cm^3 K mol^{-1} (Tb^{III}, $^7F_6$, g = 3/2), while the $\chi_M T$ value for **3** (26.25 cm^3 K mol^{-1}) is mildly larger than the value of 23.64 cm^3 K mol^{-1} for three uncoupled Gd^{III} ions ($^6S_{7/2}$, g = 2). Up cooling, the $\chi_M T$ products gradually drop to 29.99, 19.01 and 27.02 cm^3 K mol^{-1} for **1**, **3** and **4**, respectively. This behaviour should be ascribed to depopulation of the excited sublevels from the crystal-field splitting of lanthanide(III) ions and/or antiferromagnetic interactions in complexes **1**, **3** and **4**.[20] The observed $\chi_M T$ value (8.00 cm^3 K mol^{-1}) for **2** (Eu) at room temperature, is attributed to the presence of thermally populated excited states. At low temperature (1.8 K) the nonmagnetic ground state is observed with $\chi_M T$ = 0.09 cm^3 K mol^{-1}, the diamagnetic ground state of the Eu^{III} centers is thermally populated, resulting in a magnetization that is close to zero, as expected. In an attempt to quantify the magnetic interactions of Gd(III) case, we fitted the $\chi_M T$ versus T data, using a one J coupling scheme, with only the nearest-neighbor interactions considered. Using the spin Hamiltonian $\hat{H} = -2J(\hat{s}_1\hat{s}_2 + \hat{s}_2\hat{s}_3) + g\mu_B B(\hat{s}_1 + \hat{s}_2)$ within *PHI* program,[21] we determined the exchange coupling constant to be J = -0.043 cm^{-1}, with a g value of 2.07. The exchange is thus confirmed to be antiferromagnetic and extremely weak, as observed in the majority of trinuclear Gd(III) complexes.[22] Magnetization data were obtained at varying field and temperature, as shown in Figure S4. The nonsuperposition of the M vs H/T plots (Figure 4 inset) also indicates the presence of magnetic anisotropy

and/or thermally accessible low-lying excited states. Moreover, the magnetization value at 2.0 K and 50 kOe reaches 18.1 Nβ, lower than the anticipated value of 30.0 Nβ for three Dy^{III} ions, suggesting significant anisotropy in the system (Figure S4).

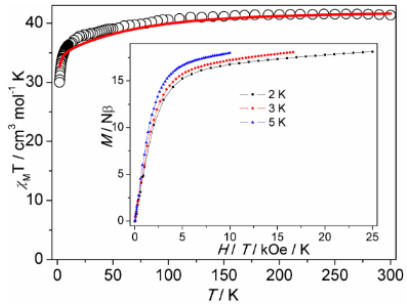

Figure 4. Plot of $\chi_M T$ vs T for **1**. Solid line represents the simulation from *ab initio* calculation. Inset: Plot of M vs H/T at different temperatures.

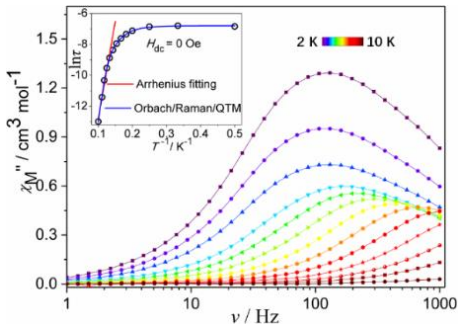

Figure 5. Frequency dependence of χ'' susceptibilities for **1** without dc field. Inset: Plot of ln τ vs T^{-1} for **1** without dc field. The red line and blue line represent the Arrhenius fit and multiple relaxation processes, respectively.

The anisotropic Dy^{III} ions in **1** could lead to single-ion-based molecular magnetic relaxation and even SMM behaviour. Therefore, alternating current (ac) magnetic susceptibility experiment for complex **1** was carried out under a zero dc field. The χ'' versus T plots were performed in the range 1.8-15 K with the frequencies of 1, 10, 33, 100, 333, and 1000 Hz, both the in-phase (χ') and out-of-phase (χ'') signals of dynamic susceptibility present strong frequency and temperature dependence. As shown in Figure S5, the in-phase and out-of-phase susceptibilities in **1** reveal significant temperature dependent peaks below 10 K. The character definitely symbolizes the slow relaxation of magnetization. Upon cooling, χ' and χ'' raise again at lower temperatures, such a situation could be due to quantum tunneling of the magnetization (QTM) which often occurs in lanthanide SMMs.[23] Then, the frequency dependencies of the ac susceptibility for complex **1** were characterized under zero dc field at various temperatures (Figures 5 and S6), the peaks of the χ'' ac susceptibility gradually move from low frequency to high frequency, explicating that the χ'' of **1** always manifests frequency dependence in selected temperature range. A simultaneous fit to a generalized Debye model for the χ' and χ'' data was used to extract magnetic relaxation times. The inset of Figure 5 shows the plot of ln(τ) vs T^{-1} for **1**. The anisotropy barrier is extracted by fitting the plots with Arrhenius analysis [$\tau = \tau_0 \exp(U_{eff}/k_B T)$] in the high temperature. The effective energy barrier (U_{eff}) and extrapolated relaxation times (τ_0) are extracted to be 126.0 K and 9.0×10^{-10} s for **1**, which are within the range expected for a SMM[24] (10^{-6}-10^{-11}). Noteworthily, the ln(τ) vs T^{-1} product for **1** appears to display a certain extent of curvature and temperature-independence at low temperature range, pointing out the effect of other possible relaxation pathways.[25] The data could be fitted considering temperature independent quantum tunnelling, thermally activated Orbach and Raman processes, using the following equation eq (1):

$$\tau^{-1} = {\tau_{QTM}}^{-1} + CT^n + {\tau_0}^{-1}\exp(-U_{eff}/kT) \quad (1)$$

To avoid the overparameterization problem, the U_{eff} value (126.0 K) is fixed in the fitting process. The best fitting gives $\tau_0 = 1.04 \times 10^{-11}$ s, $C = 0.87$, n = 3.92 and $\tau_{QTM} = 1.18 \times 10^{-3}$ s ($R^2 = 0.999$) (Figure 5 inset). The Cole-Cole plots based on frequency-dependent ac susceptibility data for **1** could be modelled by the Debye model (Figure 6).[26] The parameter α is below 0.24 from 2.0 to 7 K, consistent with values observed for Dy-based SMMs, which suggested a relatively narrow distribution of relaxation times for a single relaxation process (Table S11). Thus, complex **1** presents typical of slow magnetic relaxation in the absence of dc field. Such a phenomenon is rarely observed for the reported Dy-based MOFs possessing high-dimensional structural framework. More notably, the present case gives rise to an unexpected SMM property with highest effective energy barrier that exceed those described for all previous Dy^{III}-MOF SMMs (Table 2). On measuring the diluted sample **1@Y**, under zero dc field, the temperature-dependent ac susceptibilities show slightly differences with the looming peaks of the χ'' plots at low frequencies (Figure S7), supporting the single-ion anisotropy rather than the long-range ordering or dipolar interactions responsible for the dynamic magnetic behaviours.

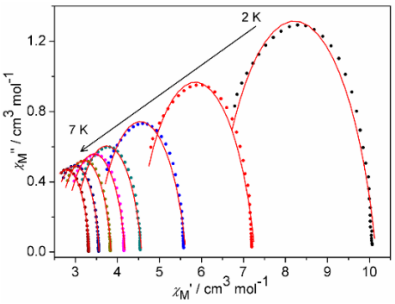

Figure 6. Cole-Cole plots for **1** at 0 Oe. The solid lines represent the best fit to the measured results.

Table 2. Dysprosium(III)-based single-molecule magnets with 3D MOFs.

Molecular formula	Unit	Configuration (coordination geometry)	U_{eff}/K	DC field/Oe	Ref
$[Dy_3(pta)_4(Hpta)(H_2O)]\cdot 6H_2O$	trinuclear	Muffin (*Cs*)	126.0	0	this work
$\{[Dy(DMTDC)_{1.5}(H_2O)_2]\cdot 0.5DMF\cdot 0.5H_2O\}_n$	mononuclear	bicapped trigonal prism	48.29	2000	27a

$[DyL^1(H_2O)_3]\cdot 3H_2O\cdot 0.75DMF$	mononuclear	trigonal dodecahedron (D_{2d})	57	1200	27b
$[Dy(STP)(1,2\text{-bdc})]_n$	mononuclear	triangular dodecahedron (D_{2d})	55.76	0	27c
$\{[Dy(C_2O_4)_{1.5}phen]\cdot 0.5H_2O\}_n$	mononuclear	square antiprism (D_{4d})	35.5	1200	27d
$[Dy(3,4'\text{-oba})(phen)_2(ox)_{0.5}]_n$	mononuclear	trigonal dodecahedron (D_{2d})	28	2000	27e
$[DyCd_2(PIDC)(HPIDC)(H_2O)_5Cl_2]\cdot 3H_2O$	trinuclear	square antiprismatic (D_{4d})	53	1400	27f
$[DyCu(BPDC)_2(H_2O)_2Cl]\cdot 1.75H_2O$	binuclear	bicapped trigonal prism (C_{2v})	42.4	2000	27g
$[Dy_2Cu(BPDC)_3(H_2O)_4](NO_3)_2\cdot 12H_2O$	trinuclear	tricapped trigonal prism (D_{3h})	95.3	5000	27g
$[Dy_2Zn(BPDC)_3(H_2O)_4](ClO_4)_2\cdot 10H_2O$	trinuclear	tricapped trigonal prism (D_{3h})	90.91	5000	27h
$Dy(TDA)_{1.5}(H_2O)_2$	mononuclear	bicapped trigonal prism (C_{2v})	44.2	-	27i
$\{[Dy_2(FDA)_3(DMF)_2]\cdot 1.5DMF\}_n$	binuclear	biaugmented trigonal prismatic (C_{2v})	41.8	2000	27j
$[Dy_2(FDA)_3(DMF)_2(CH_3OH)]_n$	binuclear	biaugmented trigonal prismatic (C_{2v})	67.5	2000	27j

H_2DMTDC = 3,4-dimethylthieno[2,3-b]thiophene-2,5-dicarboxylic acid; H_3L^1 = biphenyl-3′-nitro-3,4′,5-tricarboxylic acid; NaSTP = sodium 2-(2,2′:6′,2″-terpyridin-4′-yl)benzenesulfonate, H_2(1,2-bdc) = benzene-1,2-dicarboxylic acid; phen = 1,10-phenanthroline; 3,4′-oba=3,4′- oxybis(benzoate), ox=oxalate; H_3PIDC=2-(Pyridin-4-yl)-1H-imidazole-4,5-dicarboxylic acid; BPDC = 4,4′-dicarboxylate-2,2′-dipyridine anion; TDA=thiophene-2,5-dicarboxylic acid anion; H_2FDA=furan-2,5-dicarboxylic acid

In order to select a proper static field, capable to suppress the QTM, the χ'' data for **1** at 2.0 K was recorded under different dc fields. The signal with significant maximum at 1200 Oe for **1** indicates the field-induced magnetic relaxation and the slowest relaxation. Therefore, the ac magnetic data for **1** were further performed under a 1200 Oe static field. The frequency-dependent ac experiments for **1** were characterized (Figure S8). Both χ' and χ'' components occur as frequency dependencies, which explicitly declares the slow magnetic relaxation, and the probable relaxation behaviour through the QTM process is substantially depressed under the extra magnetic field. Obviously, the peak values of the χ'' curves in **1** move from lower frequency to higher frequency with increasing temperature. It is worth noting that the nonlinear dependence of ln(τ) the presence of multiple relaxation pathways (Figure S9). Thereby a model including two possible relaxation processes, i.e. Raman and Orbach mechanisms, is employed to analyse the contribution to the relaxation in 1 by using eq (2):

$$\tau^{-1} = CT^{\mathrm{n}} + {\tau_0}^{-1}\exp(-U_{\mathrm{eff}}/kT) \quad (2)$$

The fitting reproduces the experimental data very well, obtaining the parameters U_{eff} = 127.8 K, $\tau_0 = 3.93 \times 10^{-11}$ s, C = 2.85 ×10^{-3}, n = 6.91 for **1**. It is observed that the two relaxation processes are synchronously responsible for the entire dynamic magnetic behaviour under an applied dc field. In addition, the ac susceptibilities for **3** and **4** are also collected (Figure S10). Unfortunately, no χ'' signals are found even at 2 K.

Theoretical investigation

To gain further insight into the structure and magnetism of **1**, complete-active-space self-consistent field (CASSCF) calculations on individual Dy^{III} fragments of Dy1, Dy2 and Dy2A for complex **1** on the basis of X-ray determined geometries have been carried out with MOLCAS 8.4[17] and SINGLE_ANISO[18] programs (see Supporting Information for details). The energy levels (cm^{-1}), g (g_x, g_y, g_z) tensors and the predominant m_J values of the lowest eight Kramers doublets (KDs) of individual Dy^{III} fragments for **1** are shown in Table S12. The m_J components for the lowest two KDs of individual Dy^{III} fragments for **1** are shown in Table S13, where the ground KD of Dy2A is mostly composed by m_J = ±15/2, and its first excited KD is mostly composed by m_J = ±13/2. But the ground KDs of Dy1 and Dy2 are both mostly composed by m_J = ±15/2, and their first excited KDs are all composed by several m_J states severely. The corresponding magnetization blocking barriers of individual Dy^{III} fragments for **1** are shown in Figure 7, where the transversal magnetic moment in the ground KD of Dy2A is 0.67×10^{-2} μ_B, and thus the quantum tunneling of magnetization (QTM) in its ground KD could be suppressed at low temperature. But the transversal magnetic moment in the ground KDs of Dy1 and Dy2 are 0.53×10^{-1} and 0.17×10^{-1} μ_B, respectively, therefore allowing a fast QTM in their ground KDs, which is well consistent with the results from the magnetic measurements. The energy differences between the lowest two KDs for three Dy fragments are 84.3, 125.6 and 214.3 cm^{-1}, respectively. Which Dy fragment is the energy barrier decided by? What's the contribution to the energy barrier of two Dy fragments? Until now, we have not understood them. It is a complex problem to deduce which compound has the higher energy barrier for such multinuclear motif. Although their magnetic anisotropies dominantly come from individual Dy^{III} ions, the Dy^{III}-Dy^{III} interactions might have more or less

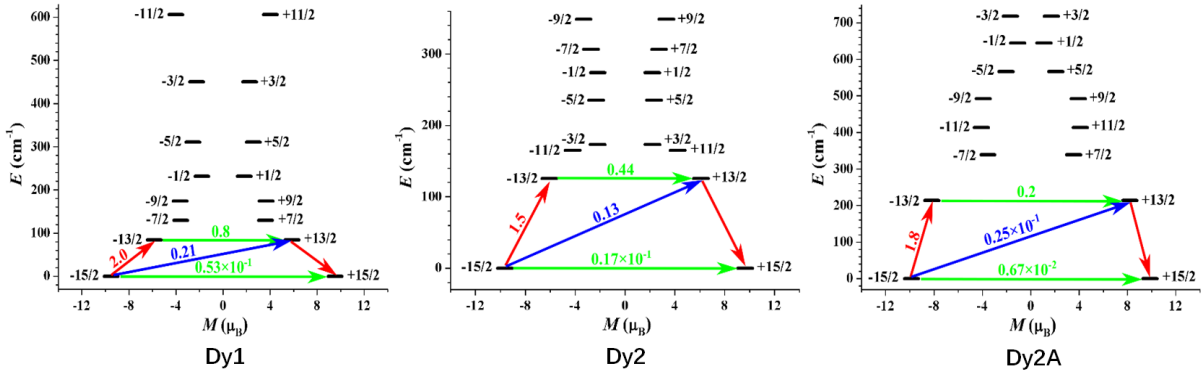

Figure 7. Magnetization blocking barriers for individual Dy^{III} fragments in **1**. The thick black lines represent the KDs as a function of their magnetic moment along the magnetic axis. The green lines correspond to diagonal quantum tunneling of magnetization (QTM); the blue line represent off-diagonal relaxation process. The path shown by the red arrows represents the most probable path for magnetic relaxation in the corresponding cites. The numbers at each arrow stand for the mean absolute value of the corresponding matrix element of transition magnetic moment.

influence on its slow magnetic relaxation process. The calculated ground g_z values of individual Dy^{III} fragments in complex **1** are close to 20, which shows that the case presents significantly axial anisotropy for Dy(III) fragments and the Dy^{III}-Dy^{III} exchange interactions can be approximately regarded as the Ising type. The program POLY_ANISO[28] was used to obtain the parameters in Table S14 fitted through comparison of the computed and measured magnetic susceptibilities (Figure 8).

The parameters from Table S14 were calculated with respect to the pseudospin $\tilde{S}_{Dy}$ = 1/2 of Dy^{III} ions. For complex **1**, the dipolar magnetic coupling constants $\tilde{J}_{dip}$ were calculated exactly, while the exchange coupling constants $\tilde{J}_{exch}$ were fitted through comparison of the computed and measured magnetic susceptibilities using the POLY_ANISO program. The calculated and experimental $\chi_M T$ versus T plot of complex **1** was shown in Figure 4, where the fit has some deviation from the experiment.[29] From Table S14, the J_1 and J_2 in **1** within Lines model[28] are both negative indicating the Dy1-Dy2 and Dy1-Dy2A interactions are antiferromagnetic, and the Dy2-Dy2A interaction of J_3 is weak ferromagnetic. We gave the exchange energies, the energy differences between each exchange doublet Δ_t and the main values of the g_z for the lowest two exchange doublets of **1** in Table S15. The main magnetic axes of three Dy^{III} ions in **1** are indicated in Figure 9, where the included angle between the magnetic axes on Dy2 and Dy2A is 92.9 °, and that between the axes on Dy1 and Dy2A is 140.4 °. Such relatively large angles suggest that the transversal components of the dipolar field caused by the Dy^{III} ions on each other are considerable, generating an important influence on the tunneling gap of individual Dy^{III} ion. The transformation of the nature or orientation of the magnetic axes seems to be corresponding to the subtle change of the coordination geometries around metal ions. Although we cannot give a clear relationship between magnetic interactions and structure details, such a special arrangement of anisotropy axes most likely contributes to a suitable overlap between lanthanide orbitals and valency orbitals of the bridging atoms to enhance the superexchange interactions between lanthanide ions in this Dy-MOF. As previous reports, the magnetic interactions between anisotropic lanthanide ions are proven to be extremely anisotropic and very sensitive to the arrangement of anisotropy axes.[30]

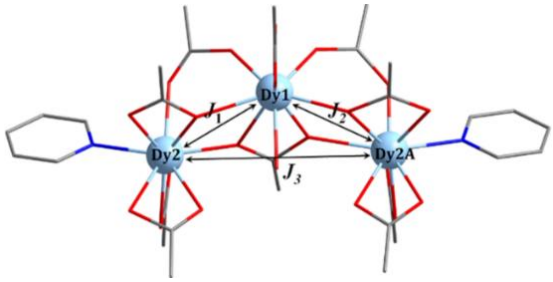

Figure 8. Scheme of the Dy^{III}-Dy^{III} interactions in **1**.

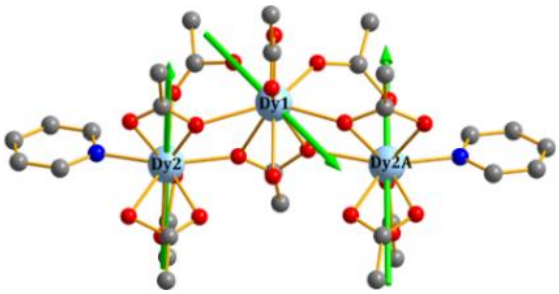

Figure 9. Calculated orientations of the local main magnetic axes on Dy^{III} ions of **1** in the ground KDs.

Magneto-structural correlations

It is well known that the coordination geometries of the crystal fields (coordination symmetry and crystal-field strength) around the paramagnetic centre play a key role in determining the magnetization dynamics. That is, the perfect axial anisotropy, which can be achieved in particular crystal field symmetries, could enormously promote the dynamic magnetic behaviour of molecular lanthanide nanomagnets. To explore the relationship between configuration and magnetic relaxation behaviours, the comparison of geometries and magnetic parameters of dysprosium(III)-based SMMs with 3D MOFs are summarized in Table 2. It can be seen that the configurations of most cases are D_{4d}, D_{2d} or C_{2v}, exhibiting slow magnetic relaxation under a zero/non-zero dc field. The energy barrier of 126 K for **1** exceeds those described for all previous Dy^{III}-MOF SMMs, which is most likely due to the unique C_s environment at the Dy^{III} centre. From the view of the coordination spheres for Dy1 and Dy2 ions, both metal centres exhibit the nine-

coordinated Muffin chromophore with different distortions from the ideal coordination geometry, on account of the minor distinction in the kinds of coordination microenvironments. The relatively small *CshMs* value for Dy1 ions corresponds to lesser deviation from ideal Muffin sphere (Table S9). On the basis of the results reported previously, in highly symmetric crystal fields, such as $C_{\infty v}$, $D_{\infty h}$, D_{4d}, D_{5h}, and D_{6d}, quantum tunneling is always well suppressed, leading to higher effective energy barrier. Existing researches also demonstrated that building the pseudo D_{4d} cage around Dy core is an elegant strategy to obtain higher effective energy barrier.[31] In present work, with the exception of the O6 atom, Dy1 exhibited the square antiprism geometry (D_{4d}) and the estimated deviation parameters is 2.222. By contrast, with the exception of the O8 atom, Dy2 is closer to the biaugmented trigonal-prismatic geometry (C_{2v}, 2.413), but it is worth noting that the calculated deviation parameter from D_{4d} is 2.542 (Figure S11 and Table S16). The difference between the parameters of C_{2v} and D_{4d} can be negligible, suggesting that the coordination geometry of Dy2 can be considered as an intermediate between C_{2v} and D_{4d}.[27j,32] Overall, the dysprosium(III) ions in **1** were enormously affected by the square antiprism geometry (D_{4d}) which is conducive to govern high energy barrier On the other hand, the exchange interaction between the lanthanide ions is also expected to contribute to the relaxation, as observed in most previous Dy^{III}-MOF SMMs (Table 2). These interaction differences might generate dissimilar anisotropy of lowest exchange multiplets, therefore affecting the uniaxial magnetic anisotropy and thermal barrier. In this work, the use of large aromatic groups has successfully weakened the interaction between adjacent trinuclear units. And the Dy^{III}-Dy^{III} interactions in the metal cluster have less influence on the slow magnetic relaxation process, which is clearly ascertained by doping operation and theoretical calculations. In spite of this, the simultaneous optimization of uniaxial anisotropy of individual Dy^{III} ions (to generate high anisotropy barriers) and magnetic interactions between the Dy^{III} ions (to suppress quantum tunnelling) are significant to achieve high-performant Dy-SMMs.

Luminescent Property

The solid-state luminescence spectra of **1**-**4** and the free H_2pta ligand were recorded at ambient temperature. Unfortunately, no emissions for **1** and **3** were observed. The ligand emissions are attributed to the π^*-π or π^*-n transition, with centred bands at 425 nm for H_2pta (λ_{ex} = 366 nm) (Figure S12). The solid-state emission spectra of **2** and **4** show the characteristic emission bands for corresponding Ln(III) ions, and all of them exhibit excellent luminescent properties with intense and narrow emission bands.

Complex **2** displays intense red luminescence and shows the characteristic emission bands for f-f transitions of europium(III) ion when excited at 320 nm (Figure 10a). The strong intensity of emission at 613 nm in the red region is derived from $^5D_0 \rightarrow {}^7F_2$ transition and the medium strong emission at 593 nm is related to the $^5D_0 \rightarrow {}^7F_1$ transition. The weak emission bands at 580 and 653 nm arise from the $^5D_0 \rightarrow {}^7F_0$ and $^5D_0 \rightarrow {}^7F_3$ transitions, respectively. The spectrum is dominated by the intense band of the $^5D_0 \rightarrow {}^7F_2$ electron dipole transition, which is the so-called hypersensitive transition and is responsible for the brilliant red emission of these complexes.

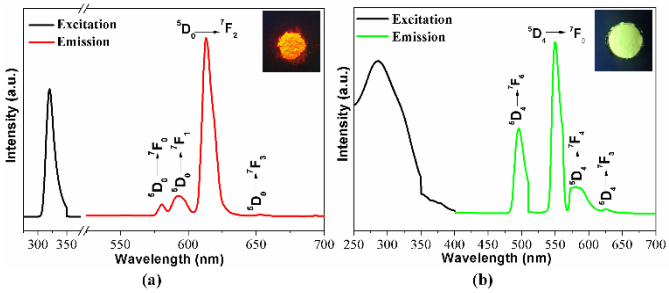

Figure 10. Solid-state photoluminescence spectra of complexes **2** (a) and **4** (b).

As can be seen in Figure 10b, under excitation of 290 nm, complex **4** governs characteristic terbium(III) emission bands, resulting from the $^5D_4 \rightarrow {}^7F_J$ (J = 6, 5, 4 and 3) transitions. The emission band at 496 nm refers to the $^5D_4 \rightarrow {}^7F_6$ transition, the strong band at 550 nm is attributed to the $^5D_4 \rightarrow {}^7F_5$ transition, the band at 582 nm corresponds to the $^5D_4 \rightarrow {}^7F_4$ transition and the band at 625 nm represents the $^5D_4 \rightarrow {}^7F_3$ transition. The fluorescence lifetime (τ) and quantum yields (Φ) are measured to be 648 μs and 7.87% for **2**, and 863 μs and 21.74% for **4**, respectively (Figure S13). Complex **4** exhibits higher quantum yields as well as luminescence lifetimes than that of complex **2** because the f–f transitions from $^5D_4$ to ^7F_J are parity- and spin-forbidden transitions.[33] It is worth noting that the emission bands of the ligands in the emission spectra of **2** and **4** are almost absent, implying that the organic ligand H_2pta is sensitized to Eu^{3+} or Tb^{3+} ions via the "antenna effect".

Conclusions

In summary, four new 3D Ln-MOFs assembled from a pyridyl dicarboxylate ligand have been synthesized. Among them, Dy-MOF is characteristic of slow relaxation of the magnetization at zero dc field with an energy barrier of 126.0 K. The magnetic behaviour of Dy-MOF is studied by a magnetic dilution method and theoretical calculations, which indicate that the thermally activated dynamic relaxation dominantly originates from the single ion anisotropy. Noteworthily, the energy barrier of Dy-MOF is superior to those of known 3D MOF-based Dy^{III} complexes. The fluorescent investigation of Eu^{III} and Tb^{III} cases demonstrates that lanthanide(III) characteristic luminescence can be generated by energy transferred to the lanthanide ions from the H_2pta ligands. This work exemplifies that the integration of lanthanide(III) cluster and multidentate pyridyl-carboxylate ligand is useful for not only yielding fascinating architectures but also enriching the potential properties.

Acknowledgements

This work was supported by NSFC (21863009, 21765017 and 21973046), the Natural Science Foundation of Ningxia Province (2020AAC02005 and 2020AAC03118), the Open Foundation of State Key Laboratory of Coordination Chemistry (SKLCC2005), and the Research Project of Ningxia Medical University

(XT2019011). Thanks are extended to the "2019 Post-doctoral Junior Leader-Retaining Fellowship, la Caixa Foundation" (J. F.-S.) (ID100010434; code: LCF/BQ/PR19/11700011). E.P. acknowledges the financial support of the European Research Council under the European Union's Horizon 2020 research and innovation programme / ERC Grant Agreement No 814804, MOF-reactors.

Conflicts of interest

There are no conflicts of interest to declare.

References

1 (a) J. Ferrando-Soria, J. Vallejo, M. Castellano, J. MartínezLillo, E. Pardo, J. Cano, I. Castro, F. Lloret, R. Ruiz-García and M. Julve, *Coord. Chem. Rev.*, 2017, **339**, 17-103; (b) B. M. Day, F.-S. Guo and R. A. Layfield, *Acc. Chem. Res.*, 2018, **51**, 1880-1889; (c) X.-Y. Liu, L. Sun, H.-L. Zhou, P.-P. Cen, X.-Y. Jin, G. Xie, S.-P. Chen and Q.-L. Hu, *Inorg. Chem.*, 2015, **54**, 8884–8886; (d) R. Sessoli, D. Gatteschi, A. Caneschi and M. A. Novak, *Nature*, 1993, **365**, 141–143;

2 (a) K. Liu, X. Zhang, X. Meng, W. Shi, P. Cheng and A. K. Powell, *Chem. Soc. Rev.*, 2016, **45**, 2423-2439; (b) X.-Y. Liu, X.-F. Ma, W.-Z. Yuan, P.-P. Cen, Y.-Q. Zhang. J. Ferrando-Soria, S.-P. Chen, E. Pardo. *Inorg. Chem.*, 2018, **57**, 14843–14851; (c) D. N. Woodruff, R. E. P. Winpenny and R. A. Layfield, *Chem. Rev.*, 2013, **113**, 5110–5148;

3 P. Zhang, Y.-N. Guo and J. Tang, *Coord. Chem. Rev.*, 2013, **257**, 1728-1763.

4 (a) R. Vincent, S. Klyatskaya, M. Ruben, W. Wernsdorfer and F. Balestro, *Nature*, 2012, **488**, 357-360; (b) T. Komeda, H. Isshiki, J. Liu, Y.-F. Zhang, N. Lorente, K. Katoh, B. K. Breedlove and M. Yamashita, *Nat. Commun.*, 2011, **2**, 217-223; (c) Y.-W. Wu, D.-N. Tian, J. Ferrando-Soria, J. Cano, L. Yin, Z.-W. Ouyang, Z.-X. Wang, S.-C. Luo, X.-Y. Liu, E. Pardo. *Inorg. Chem. Front.*, 2019, **6**, 848-856.

5 F.-S. Guo, B. M. Day, Y.-C. Chen, M.-L. Tong, A. Mansikkamäki and R. A. Layfield, *Science,* 2018*,* **362***,* 1400-1403.

6 C. A. P. Goodwin, F. Ortu, D. Reta, N. F. Chilton and D. P. Mills, *Nature*, 2017, **548**, 439-442.

7 (a) X.-Y. Liu, F.-F. Li, X.-H. Ma, P.-P. Cen, S.-C. Luo, Q. Shi, S.-R. Ma, Y.-W. Wu, C.-C. Zhang, Z. Xu, W.-M. Song, G. Xie and S.-P. Chen, *Dalton Trans.*, 2017, **46**, 1207–1217; (b) X.-H. Ma, C. Cai, W.-J. Sun, W.-M. Song, Y.-L. Ma, X.-Y. Liu, G. Xie, S.-P. Chen and S.-L. Gao, *ACS Appl. Mater. Interfaces*, 2019, **11**, 9233–9238; (c) D. D. Yin, Q. Chen, Y. S. Meng, H. L. Sun, Y. Q. Zhang and S. Gao, *Chem. Sci*., 2015, **6**, 3095-3101.

8 Q.-Y. Liu, Y.-L. Li, Y.-L. Wang, C.-M. Liu, L.-W. Ding and Y. Liu, *CrystEngComm*, 2014, **16**, 486–491.

9 (a) K. Davies, S. A. Bourne and C. L. Oliver, *Cryst. Growth Des.*, 2012, **12**, 1999-2003; (b) S.-L. Cai, S.-R. Zheng, Z.-Z. Wen, J. Fan and W.-G. Zhang, *CrystEngComm*, 2012, **14**, 8236-8243.

10 (a) Q. Zhou, F. Yang, B.-J. Xin, G. Zeng, X.-J. Zhou, K. Liu, D.-X. Ma, G.-H. Li, Z. Shi and S.-H. Feng, *Chem. Commun.*, 2013, **49**, 8244-8246; (b) S. Mohapatra, B. Rajeswaran, A. Chakraborty, A. Sundaresan and T. K. Maji, *Chem. Mater.*, 2013, **25**, 1673-1679.

11 B. Joarder, A. K. Chaudhari, G. Rogez and S. K. Ghosh, *Dalton Trans.*, 2012, **41**, 7695-7699.

12 (a) L. Jia, Q. Chen, Y.-S. Meng, H.-L. Sun and S. Gao, *Chem. Commun.*, 2014, **50**, 6052-6055; (b) S.-J. Liu, J.-P. Zhao, W.-C. Song, S.-D. Han, Z.-Y. Liu and X.-H. Bu, *Inorg. Chem.*, 2013, **52**, 2103-2109; (c) J.-M. Tian, B. Li, X.-Y. Zhang, X.-L. Li and J.-P. Zhang, *Dalton Trans.*, 2013, **42**, 8504-8511.

13 (a) S. V. Eliseeva and J.-C. G. Bünzli, *Chem. Soc. Rev.*, 2010, **39**, 189−227; (b) Y. Cui, Y. Yue, G. Qian and B. Chen, *Chem. Rev.*, 2012, **112**, 1126−1162.

14 (a) J.-H. Jia, Q.-W. Li, Y.-C. Chen, J.-L. Liu, and M.-L. Tong, *Coord. Chem. Rev.*, 2019, **378**, 365−381; (b) S.-I. Ohkoshi, S. Chorazy, M. Rams, K. Nakabayashi and B. Sieklucka, *Chem. - Eur. J.*, 2016, **22**, 7371−7375; (c) X. Yi, K. Bernot, F. Pointillart, G. Poneti, G. Calvez, C. Daiguebonne, O. Guillou, and R. Sessoli, *Chem. - Eur. J.*, 2012, **18**, 11379−11387.

15 G. M. Sheldrick, SADABS, Program for Empirical Absorption Correction for Area Detector Data, University of Göttingen, Göttingen, Germany, 1996.

16 G. M. Sheldrick, Acta Crystallogr. *Sect. C: Struct. Chem.*, 2015, **71**, 3-8.

17 (a) F. Aquilante, L. De Vico, N. Ferré, G. Ghigo, P.-Å. Malmqvist, P. Neogrády, T. B. Pedersen, M. Pitonak, M. Reiher, B. O. Roos, L. Serrano-Andrés, M. Urban, V. Veryazov and R. J. Lindh, *Comput. Chem.*, 2010, **31**, 224–247; (b) V. Veryazov, P.-O. Widmark, L. Serrano-Andres, R. Lindh and B. O. Roos, *Int. J. Quantum Chem.*, 2004, **100**, 626–635; (c) G. Karlström, R. Lindh, P.-Å. Malmqvist, B. O. Roos, U. Ryde, V. Veryazov, P. O. Widmark, M. Cossi, B. Schimmelpfennig, P. Neogŕady and L. Seijo, *Comput. Mater. Sci.*, 2003, **28**, 222–239.

18 (a) L. F. Chibotaru, L. Ungur and A. Soncini, *Angew. Chem. Int. Ed.*, 2008, **47**, 4126-4129; (b) L. Ungur, W. Van den Heuvel and L.F. Chibotaru, *New J. Chem.*, 2009, **33**, 1224-1230; (c) L. F. Chibotaru, L. Ungur, C. Aronica, H. Elmoll, G. Pilet and D. Luneau, *J. Am. Chem. Soc.*, 2008, **130**, 12445-12455.

19 M. Llunell, D. Casanova, J. Cirera, P. Alemany and S. Alvarez, *SHAPE, v2.1*, 2013.

20 J. Xiong, H.-Y. Ding, Y.-S. Meng, C. Gao, X.-J. Zhang, Z.-S. Meng, Y.-Q. Zhang, W. Shi, B.-W. Wang and S. Gao, *Chem. Sci.*, 2017, **8**, 1288–1294.

21 N. F. Chilton, R. P. Anderson, L. D. Turner, A. Soncini, K. S. Murray, *J. Comput. Chem.*, 2013, **34**, 1164−1175.

22 (a) S. K. Langley, N. F. Chilton, L. Ungur, B. Moubaraki, L. F. Chibotaru, K. S. Murray, *Inorg. Chem.*, 2012, **51**, 11873−11881; (b) L. E. Sweet, L. E. Roy, F. Meng, T. Hughbanks, *J. Am. Chem. Soc.*, 2006, **128**, 10193−10201.

23 Y.-P. Dong, P.-F. Yan, X.-Y. Zou, T.-Q. Liu and G.-M. Li, *J. Mater. Chem. C*, 2015, **3**, 4407-4415.

24 F. Gao, M.-X. Yao, Y.-Y. Li, Y.-Z. Li, Y. Song and J.-L. Zuo, *Inorg. Chem.*, 2013, **52**, 6407−6416.

25 R. L. Carlin and A. J. van Duyneveldt, *Springer: New York*, 1977.

26 M. Gregson, N. F. Chilton, A. M. Ariciu, F. Tuna, I. F. Crowe, W. Lewis, A. J. Blake, D. Collison, E. J. L. McInnes, R. E. P. Winpenny and S. T. Liddle, *Chem. Sci.*, 2016, **7**, 155–165.

27 (a) S.-N. Wang, T.-T. Cao, H. Yan, Y.-W. Li, J. Lu, R.-R. Ma, D.-C. Li, J.-M. Dou and J.-F. Bai, *Inorg. Chem.*, 2016, **55**, 5139-5151; (b) R.-C. Gao, F.-S. Guo, N.-N. Bai, Y.-L. Wu, F. Yang, J.-Y. Liang, Z.-J. Li and Y.-Y. Wang, *Inorg. Chem.*, 2016, **55**, 11323-11330; (c) C. Bai, C.-T. Li, H.-M. Hu, B. Liu, J.-D. Li and G.-L. Xue, *Dalton Trans.*, 2019, **48**, 814-817.(d) C.-M. Liu, D.-Q. Zhang and D.-B. Zhu, *Chem. Commun.*, 2016, **52**, 4804-4807; (e) L.-L. Luo, X.-L. Qu, Z. Li, X. Li and H.-L. Sun, *Dalton Trans.*, 2018, **47**, 925-934; (f) X.-J. Zhang, K. Liu, Y.-M. Bing, N. Xu, W. Shi and P. Cheng, *Dalton Trans.*, 2015, **44**, 7757-7760; (g) P.-F. Shi, G. Xiong, B. Zhao, Z.-Y. Zhang and P. Cheng, *Chem. Commun.*, 2013, **49**, 2338-2340; (h) P.-F. Shi, B. Zhao, G. Xiong, Y.-L. Hou and P. Cheng, *Chem. Commun.*, 2012, **48**, 8231-8233; (i) Z. Chen, B. Zhao, P. Cheng, X.-Q. Zhao, W. Shi and Y. Song, *Inorg. Chem.*, 2009, **48**, 3493-3495; (j) K. Liu, H.-H. Li, X.-J. Zhang, W. Shi and P. Cheng, *Inorg. Chem.*, 2015, **54**, 10224-10231.

28 M. E. Lines, *J. Chem. Phys.*, 1971, **55**, 2977–2984.

29 S. K. Langley, D. P. Wielechowski, V. Vieru, N. F. Chilton, B. Moubaraki, B. F. Abrahams, L. F. Chibotaru and K. S. Murray, *Angew. Chem. Int. Ed.*, 2013, **52**, 12014-12019.

30 E. Moreno Pineda, N. F. Chilton, R. Marx, M. Dörfel, D. O. Sells, P. Neugebauer, S.-D. Jiang, D. Collison, J. van Slageren, E. J. L. McInnes and R. E. P. Winpenny, *Nat*. *Commun*., 2014, **5**, 5243.
31 A. B. Canaj, M. K. Singh, E. R. Marti, M. Damjanovic´, C. Wilson, O. Ce´spedes, W. Wernsdorfer, G. Rajaraman and M. Murrie, *Chem*. *Commun*., 2019, **55**, 5950-5953.
32 W. Cao, C. Gao, Y.-Q. Zhang, D.-D. Qi, T. Liu, K. Wang, C.- Y. Duan, S. Gao and J.-Z. Jiang, *Chem*. *Sci*., 2015, **6**, 5947-5954.
33 (a) A. P. S. Samuel, E. G. Moore, M. Melchior, J. Xu, K. N. Raymond, *Inorg*. *Chem*., 2008, **47**, 7535−7544; (b) S. Biju, M. L. P. Reddy, A. H. Cowley, K. V. Vasudevan, *Cryst*. *Growth Des*., 2009, **9**, 3562−3569.